Supplement of Biogeosciences, 20, 971–995, 2023
https://doi.org/10.5194/bg-20-971-2023-supplement

Biogeosciences Open Access EGU

Supplement of

Atmospheric deposition of reactive nitrogen to a deciduous forest in the southern Appalachian Mountains

John T. Walker et al.

Correspondence to: John T. Walker (walker.johnt@epa.gov)

S1. Comparison of Measurement Methods for Wet Deposition and Air Concentrations

Concentrations of inorganic N in precipitation

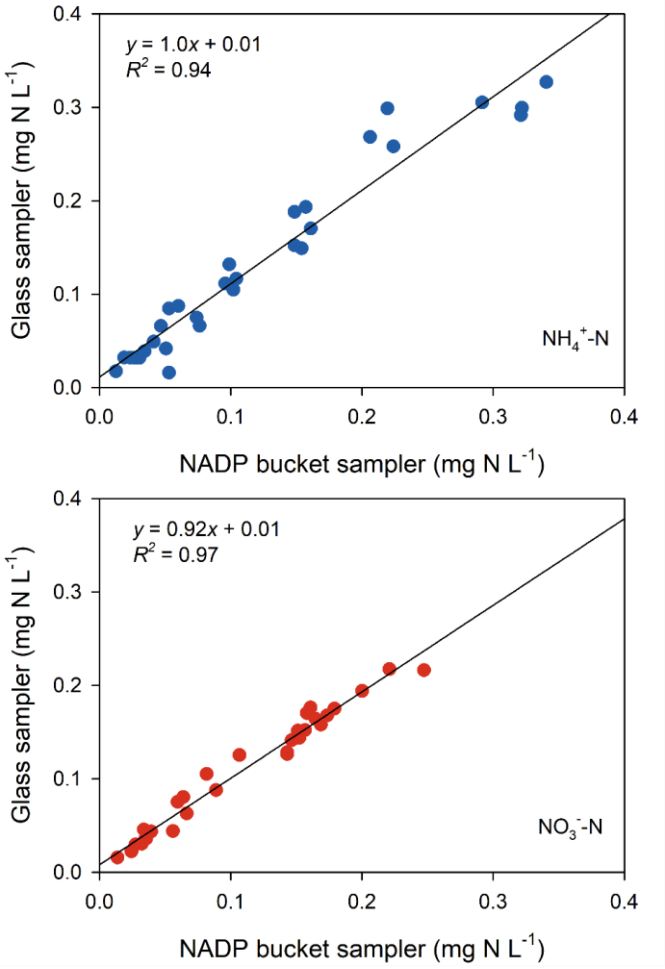

Figure S1. Comparison of NH_4^+ (top) and NO_3^- (bottom) concentrations (as N) in weekly precipitation samples between SANDS glass precipitation sampler and standard weekly NADP/NTN polyethylene bucket.

Air concentrations of HNO_3 and NH_3

HNO_3 and NH_3 were measured by several methods during SANDS (Table 2), including continuous analyzers (MARGA and TD-PC-CL) and time integrated methods (URG denuder and CASTNET). Here we briefly compared the various methods, including those that were collocated at NC25/COW137 or operated concurrently at NC25/COW137 and the eddy flux tower (EFT) (Table 1). URG denuder/filter pack results were used as reference when available. Comparison to the collocated URG denuder (3- to 4-hour integration) on the EFT showed the MARGA underestimated HNO_3 by approximately 22%, though the two methods were highly correlated (Figure S2). This underestimate could be caused by HNO_3 sorption to the MARGA inlet, which is a 30 cm length of 1.27 cm O.D. PFA tubing. Conversely, TD-PC-CL HNO_3 measured at NC25/COW137 was 23% higher than the URG denuder on

the EFT, again showing good correlation. TD-PC-CL compared well with CASTNET weekly HNO_3 concentrations (August 2015 to August 2016), particularly when considering the low weekly average concentrations observed at Coweeta.

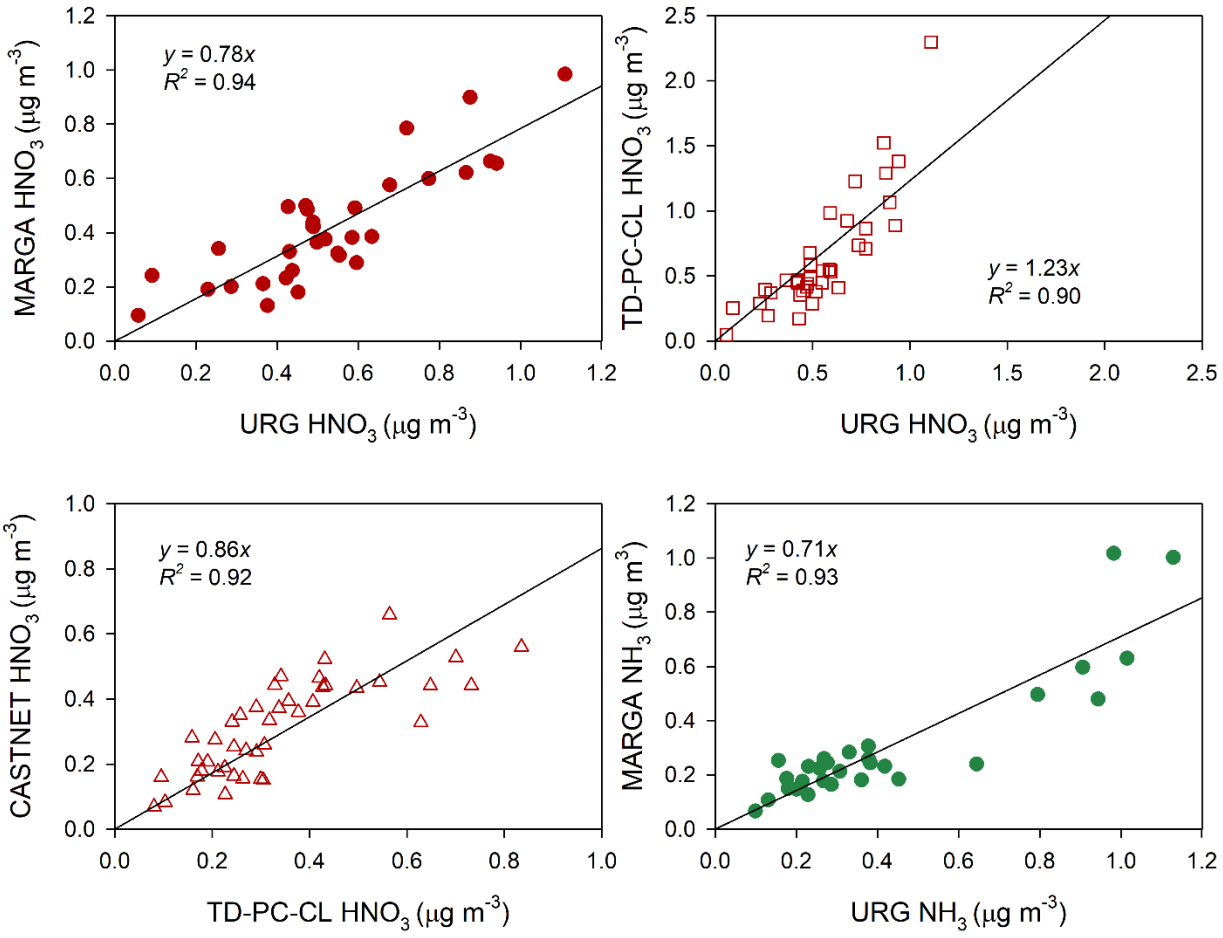

Figure S2. Comparison of HNO_3 and NH_3 measurements with regression results.

Comparison of hourly HNO_3 concentration measured by TD-PC-CL and MARGA during spring and summer 2016 is presented in Figure S3. MARGA measurements reflect a measurement heigh of 37.5m during spring and 43.5m during summer. The methods tracked very well temporally, showing diurnal patterns with a peak during the mid-day and a minimum at night. However, the MARGA consistently measured lower mid-day peak HNO_3 concentrations during both intensives. Similar to the MARGA underestimation relative to the URG denuder, this pattern may reflect loss of HNO_3 to the MARGA inlet. The disagreement is most pronounced during spring when relative humidity was higher, potentially causing more extensive sorption on tubing surfaces. Though less likely, overestimation by the TD-PC-CL method may occur if NOy species other than HNO_3 are scrubbed the KCl denuder (Section 2.2.2). Finally, the possibility that the difference between methods partly reflects real spatial differences cannot be ruled out. The MARGA system was deployed approximately 7.5 m (spring) and 13.5 m (summer) above the forest canopy

approximately 300 m to the southeast of the TD-PC-CL. The TD-PC-CL system was located in an open grassy area near the Coweeta offices and sampled from a height of 8 m above ground. Differences in dry deposition rates to the forest (higher) versus grassy area (lower) and potentially higher NO_2 concentrations (HNO_3 precursor) near the Coweeta offices may result in higher daytime HNO_3 concentrations at the TD-PC-CL location.

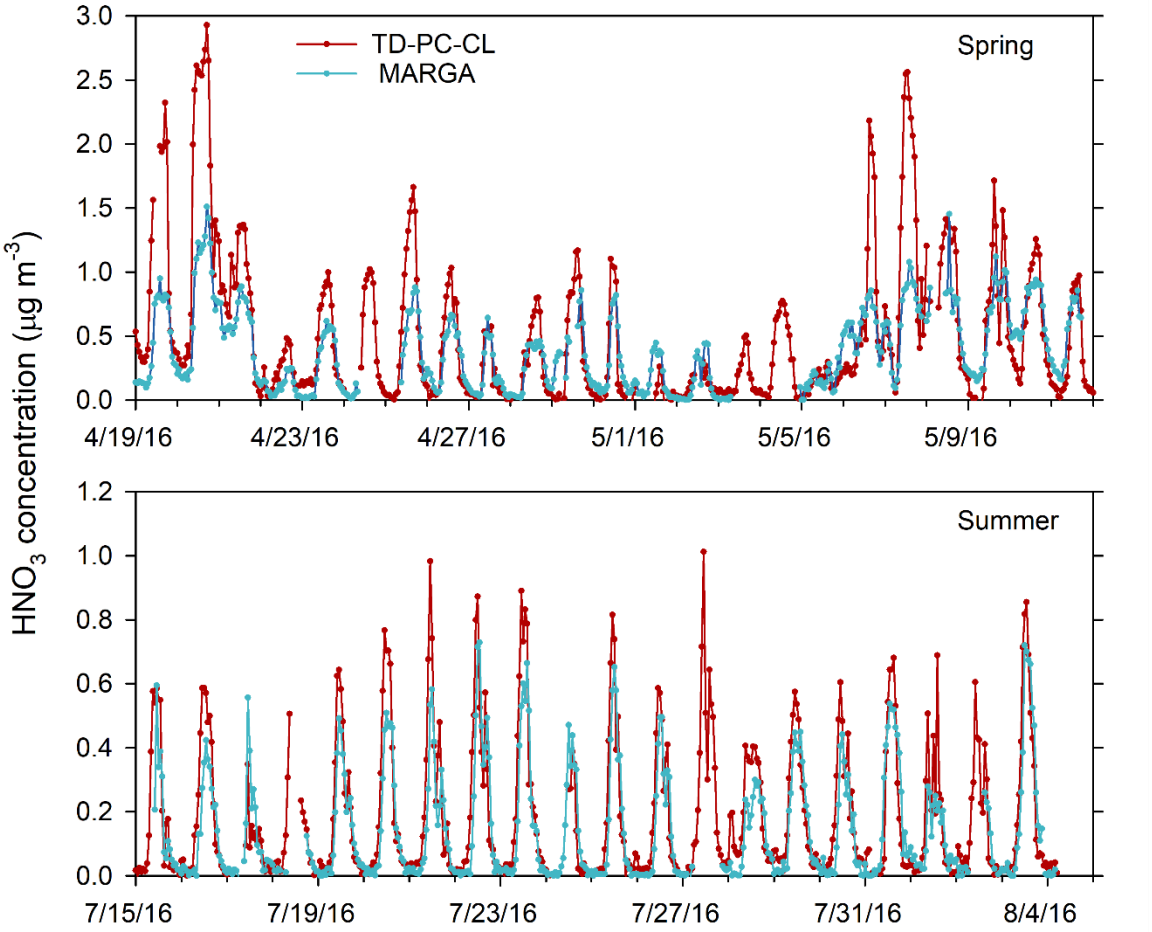

Figure S3. Time series of measured hourly HNO_3 by MARGA and TD-PC-CL during spring and summer of 2016.

Ammonia measured by the MARGA showed good correlation with the collocated URG denuder but underestimated by ~29% (Figure S2). Similar to HNO_3, this underestimation is attributed to NH_3 loss to the MARGA inlet tubing. The bi-weekly integration period of the AMoN sample, and subsequent small sample size, precludes comparison to the seasonal intensive URG and MARGA measurements.

Air concentrations of PM

Comparison of particulate SO_4^{2-} and NH_4^+ concentrations measured by Tisch Hi-Vol $PM_{2.5}$ and CASTNET samplers is presented in Figure S4. 24-hr Tisch Hi-Vol measurement data were averaged to match the weekly CASTNET measurements. Data points with completeness less than 75% were excluded from comparison. The methods compared well overall, exhibiting high correlation and offsets near zero. CASTNET concentrations were ~ 15% higher, on average, than Hi-Vol concentrations. Both methods (not shown) measured very low concentrations of NO_3^- during the periods of comparison. While typically found mostly in the fine mode, differences in SO_4^{2-} and NH_4^+ may be partly attributed to measurement of different particle sizes. CASTNET does not have a size selective inlet while the Hi-Vol measures $PM_{2.5}$. Thus, CASTNET samples some portion of the coarse particle fraction. The observation that particulate NO_3^- by CASTNET sampler was higher than the Hi-Vol (average of 0.14 and 0.018 µg m^{-3}, respectively) also suggests the collection of some coarse nitrate by CASTNET. Differences in NH_4^+ and NO_3^- may also relate to the flow rate of the two samplers. The significantly higher flow rate of the Hi-Vol sampler (230 L min^{-1}) may promote greater volatilization of NH_4NO_3 than CASTNET (1.5 L min^{-1}).

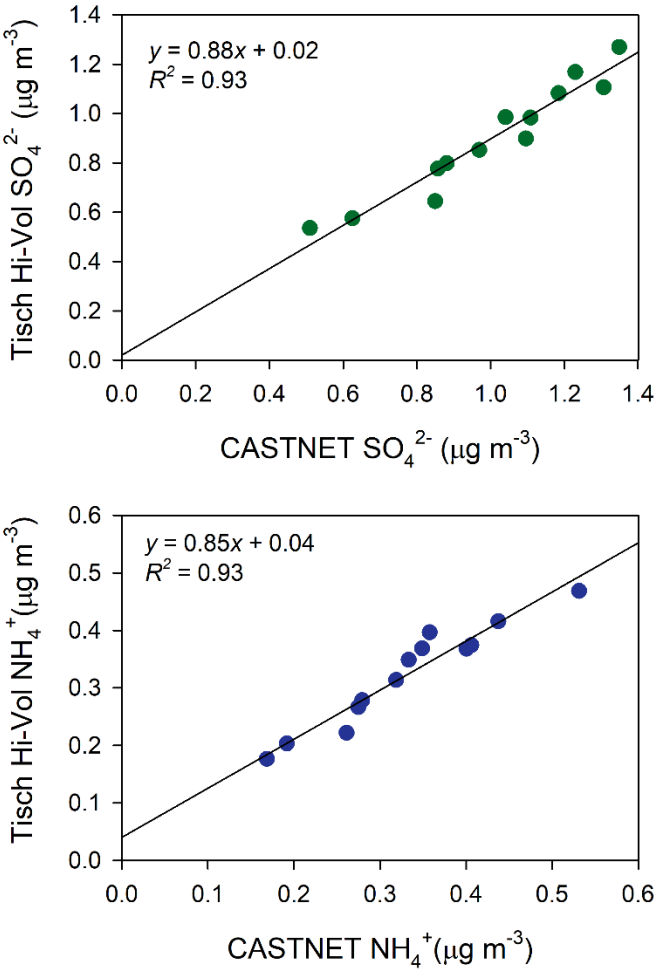

Figure S4. Comparison of particulate SO_4^{2-} and NH_4^+ concentrations measured by co-located Tisch Hi-Vol $PM_{2.5}$ and CASTNET samplers.

Passive HNO_3 sampler

In order to quantify ambient HNO_3 concentrations with the passive samplers, a calibration was conducted by comparing the passive sampler with a collocated CASTNET filter pack sampler at Screwdriver Knob. A median "effective" passive sampling rate was calculated over the full collocation period. The calibrated passive measurement is compared to the collocated filter pack measurement in Figure S5. Average(median) concentrations of the data shown in the graph are 0.1(0.1) and 0.1(0.1) µg m^{-3} for the passive and filter pack, respectively. The sampling rate was applied to the passive HNO_3 samplers deployed across the basin (Figure 1, Table 1, Figure 13).

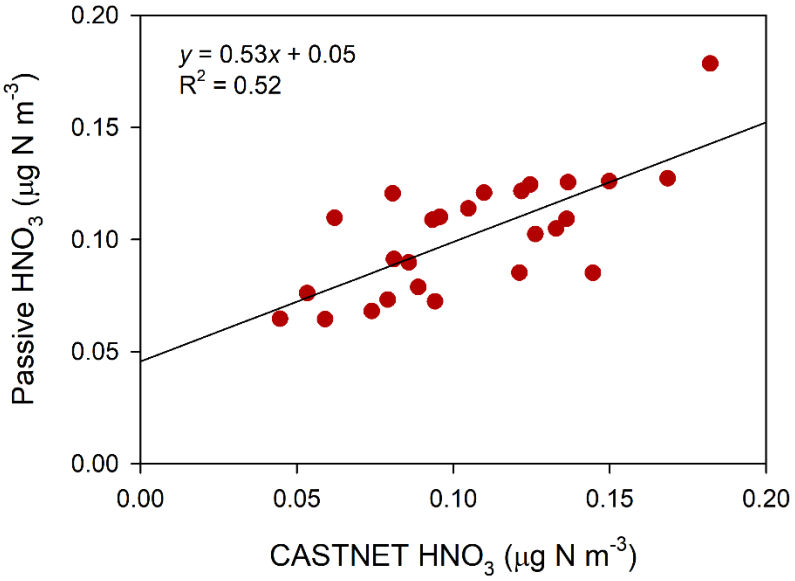

Figure S5. Comparison of calibrated passive and CASTNET HNO_3 at Screwdriver Knob

S2. TD-PC-CL Instrument

The thermal decomposition, photolytic conversion, chemiluminescence (TD-PC-CL) instrument at Coweeta used a 10 cm long 0.635 cm O.D. PFA Teflon inlet line, a 0.5 L PFA ballast tank, three 30 cm long by 0.5 cm diameter quartz converter tubes and three model BLC2 second generation blue LED converters (Air Quality Design, Inc., Wheat Ridge, CO) to sample inlet air, thermally convert total peroxy nitrates (ΣPNs) and total alkyl nitrates (ΣANs) to NO_2 and then photolyze NO_2 to NO. The inlet was mounted approximately 8 m above ground level and 5 m horizontal distance from the equipment shelter. Ambient air was drawn through a single inlet line into the ballast tank where flow was split into three separate channels. The purpose of the ballast tank was to provide approximately 16 seconds residence time to the system in order to smooth the signal as the analyzer switches between channels. Channel 1 air (baseline) flowed into a quartz converter tube maintained at shelter temperature. From there, the sample entered the pre-reactor channel of a Thermo-Environmental Model 42i NO-NOx analyzer and the ambient NO_2 plus analyzer

background signal was measured. In normal operation, the pre-reactor in the Model 42i was used to measure signal from instrument background plus non-NO interferences. For this application, the O_3 feed to the pre-reactor was disconnected so that it could function as an independent measurement channel. The baseline signal from Channel 1 measured instrumental noise, plus chemical interferences, plus NO and NO_2.

Channel 2 air was directed through a quartz converter tube heated to 180 ^oC. Air from the converter then flowed through 10 cm of 0.635 cm O.D. stainless steel tubing to cool the sample, then into a second blue LED converter and finally the NO channel of the NO-NOx analyzer. Channel 2 thus measures baseline plus ΣPNs. Channel 3 air followed an identical path, except the quartz converter was heated to 360^oC, then into the blue LED and the NOx channel of the analyzer. Channel 3 measured baseline plus ΣPNs plus ΣANs.

Prior to deployment, the NO-NOx detector was calibrated with NIST-traceable NO (Scott-Marrin, Riverside, CA) and conversion factors for the blue LEDs were determined with NO_2 (Scott-Marrin). Challenges with isopropylnitrate (Scott-Marrin) concentrations between 2 and 40 parts per billion (ppb) showed no response on either Channel 1 or Channel 2 and 96±2 % recovery on Channel 3. Post-deployment challenges with isopropylnitrate showed slightly lower recoveries on Channel 3 (i.e., 94 ±3 %).

In the field, detector responses and converter efficiencies were checked with NO and NO_2, respectively, every three days. Zero air zeros and dynamic zeros (heaters turned off) were performed every 3 days and 7 days, respectively. Both types of zeros indicated 1-sigma detection limits of 0.018-0.027 ppb. Data processing involved acquisition of signals from all three channels with 1-minute time resolution, followed by averaging to 5-minute intervals and adjustment of each channel for NO_2 response. PNs were then calculated as the difference between adjusted Channel 2 and adjusted Channel 1, and ANs were calculated as the difference between adjusted Channel 3 and adjusted Channel 2.

Table S1. Species list, basal area, and maximum leaf area index, based on allometric equations from four 25 × 25 m plots near the base of the EFT, sorted by leaf area index (Oishi et al., 2018).

Scientific name	Common name	Basal area (m^2 ha^{-1})		Leaf area index (m^2 m^{-2})	
Betula lenta L.	Black (sweet) birch	3.19	10.90%	1.05	22.60%
Liriodedron tulipifera L.	Tulip (yellow) poplar	6.94	23.80%	0.81	17.50%
Quercus alba L.	White oak	5.09	17.50%	0.65	14.00%
Rhododendron maximum L.	Great (rosebay) rhododendron	4.39	15.10%	0.6	12.90%
Acer rubrum L.	Red maple	2.18	7.50%	0.44	9.50%
Nyssa sylvatica Marsh.	Blackgum	2.06	7.10%	0.33	7.10%
Oxydendrum arboreum L. (DC.)	Sourwood	1.89	6.50%	0.27	5.80%
Carya spp.	Hickory species	0.8	2.70%	0.13	2.80%
Fagus grandifolia Ehrh.	American beech	0.62	2.10%	0.1	2.20%
Quercus velutina Lam.	Black oak	0.46	1.60%	0.08	1.70%
Cornus florida L.	Flowering dogwood	0.32	1.10%	0.05	1.10%
Kalmia latifolia L.	Mountain laurel	0.25	0.90%	0.04	0.90%
Carpinus caroliniana Walter	American hornbeam	0.19	0.70%	0.03	0.60%
Quercus rubra L.	Red oak	0.17	0.60%	0.02	0.40%
Fraxinus americana L.	White ash	0.14	0.50%	0.02	0.40%
Tsuga canadensis L.	Eastern hemlock	0.31	1.10%	0.01	0.20%
Pinus strobus L.	Eastern white pine	0.08	0.30%	0.01	0.20%
Magnolia fraseri Walter	Mountain (Fraser) magnolia	0.05	0.20%	<0.01	<0.2%
Ilex opaca Aiton	American holly	0.02	0.10%	<0.01	<0.2%
TOTAL		29.14		4.64	

S3. Above-canopy Gradient Flux Measurements

During the 2016 summer intensive a total of 19 vertical concentration profiles for reactive nitrogen compounds were measured during daytime (typically 0800 – 1700) using a glass annular denuder/filter pack (URG Corporation, Chapel Hill, NC) system as described in Section 2.2.2. The above canopy concentration gradients for HNO_3 and NH_3 were obtained from the measurements at 43 m and 34.6 m and the deposition fluxes were calculated by the MBR method. There were three and two profiles for HNO_3 and NH_3, respectively, in which the measurements at 34.6 m were missing or of poor quality. In these cases, the measurements at a lower level (32.0 m) were used to calculate the concentration gradient, although they may suffer larger uncertainty due to greater influence of roughness sublayer (canopy height = 30 m). There are one and four concentration profiles for HNO_3 and NH_3, respectively, exhibiting counter-gradient phenomenon (i.e., emission) above canopy. The sample durations of the concentration profiles were typically 3 or 4 hours. The hourly K_t values were first calculated from the hourly heat flux and temperature gradient measurements and then averaged for the 3-4 hour sample period after omitting obvious outliers (points > 3 scaled median absolute deviation (MAD) away from the median).

Table S2. Summary of resistance formulas implemented in STAGE.

Resistance component	Formulation
Aerodynamic resistance	$R_a = u/u_*^2$
Leaf boundary layer resistance	$R_{bl} = \frac{v}{u_* D_c}\left(\frac{u_* l}{v LAI^2}\right)^{1/3}$
Stomatal resistance	$R_s = \frac{r_{s,\min}}{LAI f_{PAR} f_T f_{vpd} f_w}\frac{D_{H_2O}}{D_c} + \frac{1}{LAI\left(H^*/3000 + 100 f_0\right)}$
Cuticular resistances	$R_{cut} = \left[LAI\left(\frac{f_{wetleaf}}{R_{cut,wet}} + \frac{1-f_{wetleaf}}{R_{cut,dry}}\right)\right]^{-1}$ For NH_3, $R_{cut,dry} = R_{cut,\min} e^{\alpha_{cut}(100-RH)}$ For other reactive N compounds, $R_{cut,dry} = R_{cut0}\, a_0 / f_{rel}$ $R_{cut,wet} = R_{mt} + R_{mt}/\left(W_L H^*\right)$ $R_{mt} = \left(k_{mt} r\right)^{-1}$
Total ground resistance	$R_g = R_{inc} + R_{bg} + R_{soil}$
In-canopy aerodynamic resistance	$R_{inc} = R_a\left(e^{0.5LAI} - 1\right)$
Ground boundary layer resistance	$R_{bg} = \frac{v/D_c - \ln\left(\delta_0/z_1\right)}{k u_{*g}}$
Soil resistance	For NH_3, $R_{soil} = L_{dry}/D$ For other reactive N compounds, $R_{soil} = \left(\frac{f_{wetsoil}}{R_{soil,wet}} + \frac{1-f_{wetsoil}}{R_{soil,dry}}\right)^{-1}$ $R_{soil,dry} = R_{soil0}\, a_0 / f_{rel}$ $R_{soil,wet} = R_{mt} + R_{mt}/\left(W_L H^*\right)$

Note. u = mean wind speed; u_* = friction velocity; v = kinematic viscosity of air; D_c = molecular diffusivity of a specific gas; l = length scale over which the viscous sub-layers are permitted, which is a typical leaf width; LAI = leaf area index; $r_{s,min}$ = minimum leaf stomatal resistance for water vapor; f_{PAR} = environmental stress function of radiation; f_T = environmental stress function of temperature; f_{vpd} = environmental stress function of humidity; f_w = environmental stress functions of leaf water potential; D_{H2O} = molecular diffusivities for water vapor; H^* = effective Henry's Law constant; f_0 = reactive factor; $f_{wetleaf}$ = fraction of wet canopy leaf; $R_{cut,min}$ = minimum cuticular resistance of NH_3; a_{cut} = an empirical factor; RH = relative humidity; R_{cut0} = reference value for cuticular resistance; a_0 = a constant value; f_{rel} = relative reactivity; W_L = liquid water content fraction; k_{mt} = mass transfer coefficient of a

specific gas; r = droplet radius; δ_0 = distance above ground where the eddy diffusivity is equal to molecular diffusivity; z_1 = upper height of logarithmic profile that forms above ground; u_{*g} = friction velocity at ground level; L_{dry} = soil dry layer thickness; D = gas diffusivity within soil; $f_{wetsoil}$ = fraction of wet soil surface; R_{soil0} = reference value for soil resistance.

S4. Canopy Physical Characteristics

Canopy total leaf area (m^2 m^{-2}) was estimated along a 370 m transect during the spring and summer 2016 intensives using a wide-angle canopy imager (CID Bio-science CI-110 Plant Canopy Imager) at an average spacing of 28 m between 15 image locations (Breda, 2003). The transect origin was randomly selected within the Coweeta EFT footprint, directed from the northeast to the southwest of the tower. The CI-110 (Software v1.1.71) estimates plant area index (PAI) through a gap-fraction inversion procedure (Campbell and Norman, 1998). PAI is a whole tree index, including branches, stem and leaf components of a tree. To avoid sampling and optical errors associated with view angles close to zenith and the horizon, a 30^o – 60^o zenith angle range was selected for analysis (Leblanc et al., 2005). Early morning and late evening collections ensured diffuse light conditions necessary for consistent exposure across the entire image. A species-specific woody-to-total (W:T) correction was applied to the *in situ* PAI to arrive at leaf area index (LAI) (Iiames et al., 2008). The CI-110 LAI estimates were then calibrated to LAI estimated using tree-specific allometric equations developed through destructive sampling in the Coweeta basin (Martin et al., 1998). These equations were then applied to forest stand measurements (species, density, size class) within the tower footprint to estimate LAI (Oishi et al., 2018; Table S1). The allometry based estimate of peak summer LAI (4.64 m^2 m^{-2}) shown in Table S1 was used to adjust both the CID measurements and the MODIS LAI estimates as described below.

The MODerate resolution Imaging Spectroradiometer (MODIS) global LAI product (MCD15A2H) was used to develop a continuous time series of LAI for deposition modeling. MODIS LAI estimates are generated daily at a 500 m spatial resolution and each data point covers an 8-day period. The primary MODIS algorithm solves a 3-dimensional radiative-transfer model using atmosphere-corrected MODIS spectral surface reflectance and biome identification (Myneni et al., 2002). LAI for the eddy flux tower (EFT, Figure 1, Table 1) location was estimated from values of the surrounding four grid points by using inverse distance weighted interpolation. Raw MODIS data were corrected for MODIS QC, including Cloud State, Confidence Score, Snow_Ice, Aerosol, Cirrus, Internal_Cloud Mask, and Cloud_Shadow flags then smoothed and gapfilled. After these processing steps, the summer maximum MODIS LAI at the tower site was 5.62 m^2 m^{-2}, which is higher than the allometry base estimate of 4.64 m^2 m^{-2} (Oishi et al., 2018) described above. A ratio of 0.83 was applied to scale the summer MODIS LAI to the allometry based estimate. The minimum MODIS LAI at the tower site was 0.5 m^2 m^{-2}, which is close to the allometry based LAI estimate for *Rhododendron maximum L.* (0.6 m^2 m^{-2}) shown in Table S1 and was therefore not adjusted. The daily time series of MODIS LAI used for deposition modeling is shown in Figure S6 along with the spring and summer CID transect measurements of total LAI described above. The CID measurements are included to illustrate variability in LAI across the landscape surrounding the tower.

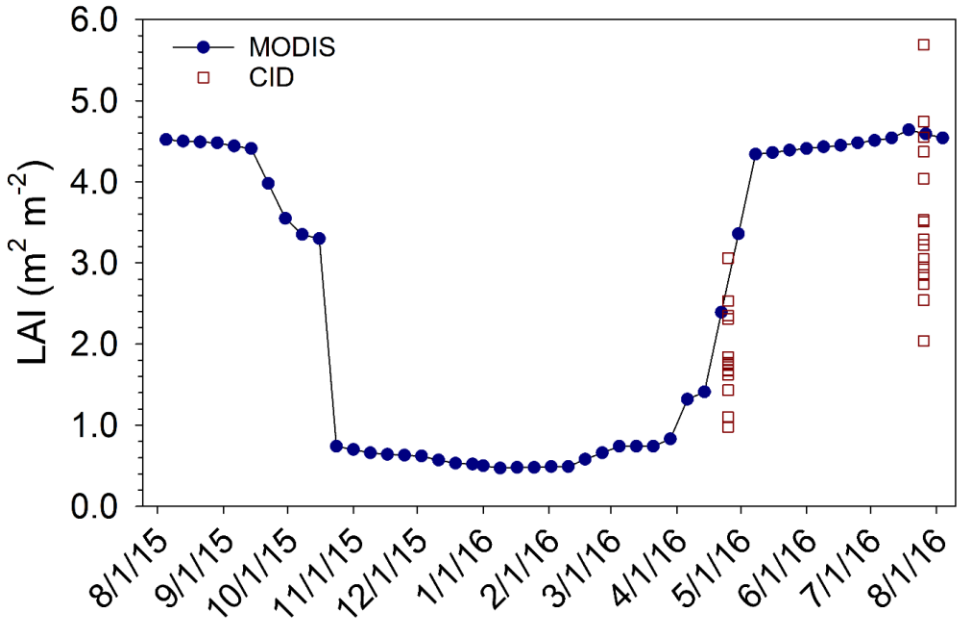

198

199 **Figure S6. Time series of MODIS LAI used for deposition modeling and transect CID LAI measurements.**

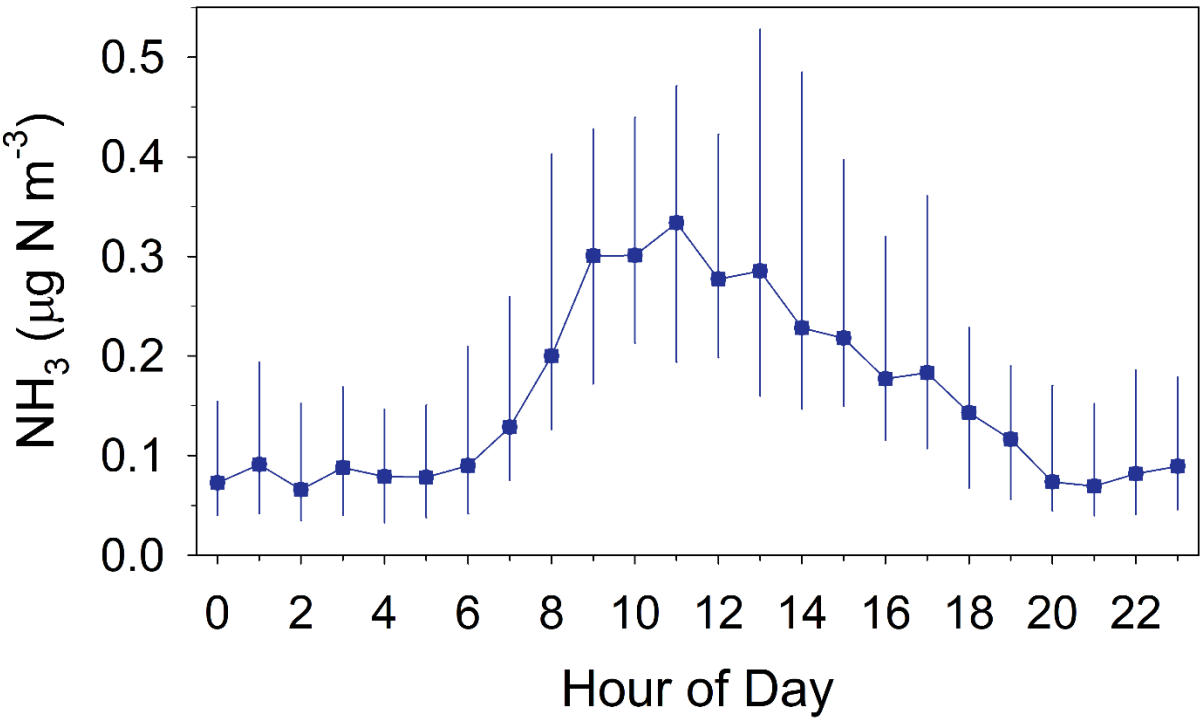

200

201 **Figure S7. Diel profile of NH_3 concentration measured by the MARGA. Data from spring and summer 2016**
202 **intensives are combined. Observations represent median hourly concentration and bars represent**
203 **interquartile range (~ 60 observations in each hourly bin).**

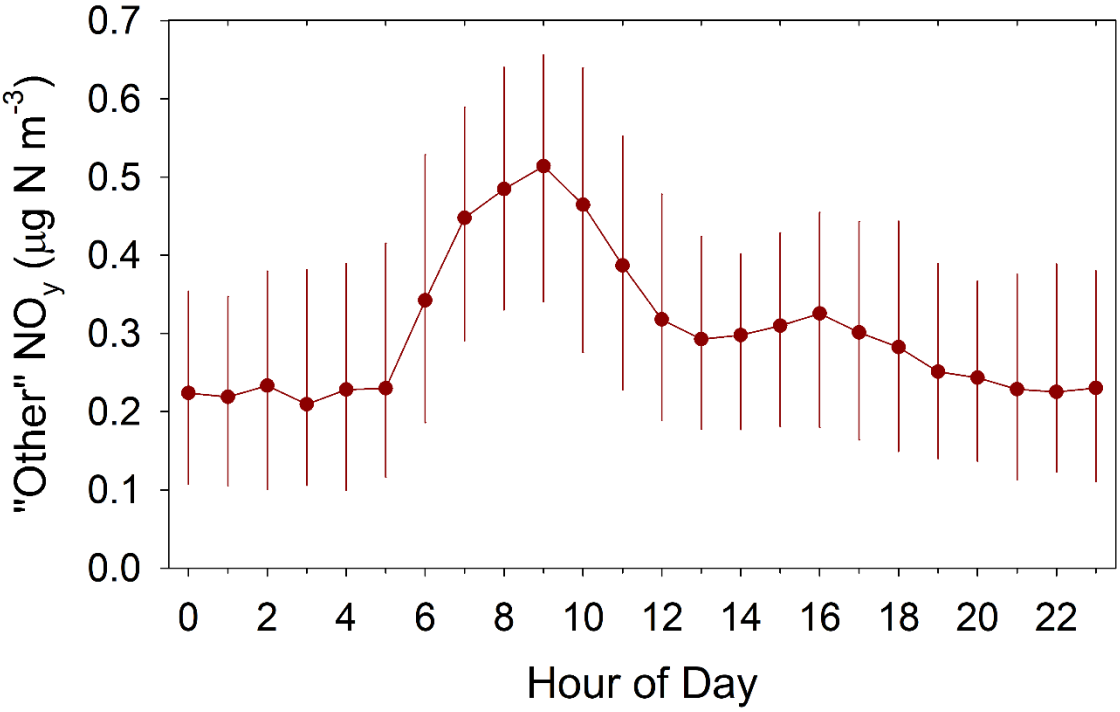

Figure S8. Diel profile of measured "Other" NOy (i.e., NO_y – HNO_3 – ΣPN – ΣAN). Observations represent median hourly concentration and bars represent interquartile range.

Table S3. Summary of options used in the Community Multi-scale Air Quality (CMAQ V5.2.1) model and coupled Weather Research and Forecasting (WRF) meteorological model.

WRF Model options	
WRF version	V3.8
Land cover data set	NLCD 2011
Land-surface model	Pleim-Xiu
Data assimilation	Four-Dimensional Data Analysis (FDDA) with no nudging in the PBL
Microphysics module	Morrison double-moment
Radiation module	Rapid Radiative Transfer Model Global (RRTMG)
Convective parameterization	Kain-Fritsch
Lightning data assimilation	Yes
MCIP post-processing	V4.3
CMAQ Model options	
CMAQ version	V5.2.1
Chemical mechanism	CB6r3
Aerosol module	CMAQ Aerosol Module version 6 (AE6)
Deposition module	M3DRY
Lightning NOx	Yes
Bidirectional NH3 flux	Yes
Emissions platform	2015fd
Boundary conditions	CMAQ v5.2 hemispheric model

Table S4. Summary of NH_4^+, NO_3^-, NO_2^-, and WSON concentrations in precipitation (μg N L^{-1}) and % contribution to WSTN. *N* = 52 observations.

		Mean	Median	S.D.	Q1	Q3	Min.	Max.
Concentration	NH_4^+	204.6	130.1	263.5	66.0	297.0	16.0	1808.9
μg N L^{-1}	NO_3^-	147.9	133.9	109.2	71.7	176.0	15.7	611.4
	NO_2^-	1.1	0.5	1.8	0.0	1.2	0.0	8.4
	WSON	51.6	25.7	94.8	10.8	53.6	0.1	559.6
%WSTN	NH_4^+	47.0	46.8	8.3	41.0	51.9	26.9	73.9
	NO_3^-	41.7	42.2	8.3	36.3	46.7	21.0	58.7
	NO_2^-	0.3	0.2	0.5	0.0	0.4	0.0	2.5
	WSON	11.0	9.4	7.7	6.1	13.8	0.1	38.0

Table S5. Summary of seasonal and annual measured NOy, HNO_3, ΣPN, ΣAN concentrations (μg N m^{-3}). S.D. represents 1 standard deviation, Q1 and Q3 represent 1st and 3rd quartiles (interquartile range), respectively, and *N* represents the number of observations.

	Period	NO_y	HNO_3	ΣPN	ΣAN
Mean	*Winter*	0.749	0.065	0.045	0.042
	Spring	0.667	0.120	0.068	0.056
	Summer	0.341	0.067	0.053	0.055
	Fall	0.425	0.040	0.046	0.036
	Annual	0.553	0.076	0.055	0.049
Median	*Winter*	0.626	0.042	0.033	0.029
	Spring	0.597	0.071	0.053	0.047
	Summer	0.299	0.032	0.041	0.047
	Fall	0.351	0.019	0.033	0.026
	Annual	0.463	0.039	0.039	0.037
S.D.	*Winter*	0.543	0.066	0.039	0.042
	Spring	0.364	0.128	0.058	0.042
	Summer	0.216	0.076	0.044	0.040
	Fall	0.308	0.050	0.038	0.033
	Annual	0.416	0.093	0.047	0.041
Q1	*Winter*	0.413	0.018	0.018	0.015
	Spring	0.396	0.026	0.026	0.024
	Summer	0.165	0.013	0.023	0.025
	Fall	0.188	0.008	0.018	0.014
	Annual	0.264	0.015	0.021	0.019
Q3	*Winter*	0.924	0.093	0.060	0.053
	Spring	0.866	0.180	0.097	0.077
	Summer	0.470	0.100	0.072	0.078
	Fall	0.566	0.054	0.065	0.048
	Annual	0.725	0.107	0.075	0.067
N	*Winter*	2002	1884	1783	1773
	Spring	2108	2016	1836	1825
	Summer	2105	1956	2049	2023
	Fall	1477	1379	1233	1229
	Annual	7692	7235	6901	6850

Table S6. Mean seasonal and annual percent (%) contribution of measured HNO_3, ΣPN, ΣAN, and "Other" compounds to total NOy. Other NOy is calculated at NO_y – HNO_3 – ΣPN – ΣAN. Number of hourly observations (*N*) is also shown.

	Other NO_y	HNO_3	ΣPN	ΣAN	*N*
Winter	75.8	8.6	8.1	7.5	1723
Spring	61.7	16.0	11.4	11.0	1777
Summer	47.1	16.2	16.7	20.0	1925
Fall	68.5	8.6	12.1	10.9	1160
Annual	62.3	12.8	12.2	12.7	6585

Table S7. Summary of NH_4^+, NO_3^-, NO_2^-, and WSON concentrations in Hi-Vol $PM_{2.5}$ samples and % contribution to WSTN. *N* = 103 observations.

		Mean	Median	S.D.	Q1	Q3	Min.	Max.
Concentration	NH_4^+	0.264	0.248	0.123	0.192	0.331	0.076	0.795
μg N m^{-3}	NO_3^-	0.004	0.003	0.004	0.002	0.005	0.000	0.020
	NO_2^-	0.001	0.001	0.001	0.000	0.001	0.000	0.007
	WSON	0.037	0.026	0.036	0.010	0.054	0.000	0.140
%WSTN	NH_4^+	86.8	89.5	10.2	81.4	94.7	51.4	100.0
	NO_3^-	1.4	0.9	1.4	0.6	1.8	0	7.0
	NO_2^-	0.3	0.2	0.4	0.1	0.3	0	3.6
	WSON	11.5	9.1	10.0	3.9	17.5	0	45.4

Table S8. Statistical summary of green leaf, senescent leaf and litter tissue chemistry along with Γ calculated from tissue chemistry.

		Mean	S.D.	Median	P25	P75	Min	Max	*N*
Green Leaves	pH	4.7	0.7	4.6	4.2	5.4	3.0	6.3	75
	NH_4^{+*}	66.3	65.6	47.0	12.7	105.0	0.1	294.0	75
	Γ	267.0	630.4	35.8	10.3	171.0	0.0	4070.0	75
Senescent Leaves	pH	4.6	0.6	4.6	4.2	4.9	3.5	5.7	21
	NH_4^{+*}	346.2	338.0	186.0	72.7	637.0	23.5	1110.0	21
	Γ	784.5	1698.8	113.0	52.2	525.0	3.4	7370.0	21
Litter	pH	5.1	0.6	5.0	4.5	5.5	3.9	6.1	65
	NH_4^{+*}	44.6	24.4	36.8	26.4	58.2	11.5	104.7	65
	Γ	314.7	464.7	69.3	26.0	494.2	4.9	2197.2	65

*μg NH_4^+ g fresh tissue^{-1}

Table S9. Median statistics and number of observations of tissue chemistry for individual green leaf samples by species. Note single observations for Sassafras and Eastern Hemlock.

Scientific Name	Common Name	*N*	pH	NH_4^{+*}	Γ
Acer rubrum L.	Red maple	9	4.2	156.0	46.4
Betula spp.	Birch species	1	3.9	7.1	1.0
Carya spp.	Hickory species	5	4.4	93.9	44.2
Fagus grandifolia Ehrh.	American beech	6	4.7	20.3	29.7
Ilex opaca Aiton	American holly	3	5.4	110.0	613.0
Kalmia latifolia L.	Mountain laurel	4	5.2	5.6	32.9
Liriodedron tulipifera L.	Tulip (yellow) poplar	7	5.7	129.0	1750.0
Magnolia fraseri Walter	Mountain (Fraser) magnolia	3	5.6	23.7	313.0
Oxydendrum arboreum L. (DC.)	Sourwood	4	3.2	6.4	0.3
Pinus strobus L.	Eastern white pine	3	4.1	21.7	6.8
Quercus alba L.	White oak	9	4.5	25.3	23.5
Quercus coccinea L.	Scarlet oak	4	4.3	37.5	13.4
Quercus prinus L.	Chestnut oak	3	5.4	139.0	719.0
Quercus velutina Lam.	Black oak	5	4.5	52.6	44.4
Rhododendron maximum L.	Great (rosebay) rhododendron	7	5.2	4.2	14.6
Sassafras albidum (Nutt.)	Sassafras	1	5.8	91.9	1090.0
Tsuga canadensis L.	Eastern hemlock	1	3.6	10.0	0.8

*NH_4^+ (μg g fresh tissue^{-1})

Table S10. Statistical summary of hourly modeled deposition velocities (cm s^{-1}) for individual N compounds (*N* = 8784).

	Mean	S.D	Median	Q1	Q3
NH_3	1.58	1.23	1.30	0.72	2.16
NH_4^+	0.08	0.09	0.05	0.03	0.10
HNO_3	3.13	1.99	2.75	1.63	4.22
NO_3^-	0.07	0.07	0.04	0.02	0.08
NO_2	0.16	0.21	0.07	0.03	0.15
AN	0.52	0.57	0.29	0.21	0.56
PN	0.32	0.15	0.26	0.21	0.39
PON	0.07	0.08	0.04	0.02	0.08

S5. Sensitivity of Dry Deposition to Model Parameterizations

Sensitivity tests of dry deposition model parameterizations are summarized in Table S11. Leaf area index is a key model input, as fluxes of all species scale with the canopy surface area available for dry deposition. In our analysis we use LAI derived from MODIS for the annual dry deposition simulation (Supplemental Figure S6). Ground-based measurements of LAI along transects in the vicinity of the forest flux tower show large spatial variability, with individual values scattering around the MODIS estimate. The sensitivity of the modeled dry deposition to LAI is evaluated by adjusting LAI in the base case simulation by ± 30%, equivalent to the mean of the ground-based observations ± the relative standard deviation. Increasing LAI by 30% from the base case increases total dry deposition by 0.33 kg ha^{-1} (+12.5%), increasing the contribution of dry to total deposition from 39.5% to 42.2%. Decreasing LAI by 30% reduces total dry N deposition by 0.38 kg ha^{-1} (-14.4%), subsequently reducing the contribution of dry to total deposition from 39.5% to 35.8%.

As the dominant deposition pathway for NH_3, it is important to understand the sensitivity of the model results to the cuticular resistance parameterization (R_{cut}, Table S2). The cuticular resistance for NH_3 is typically parameterized as a function of LAI, surface wetness, and the amount of NH_3 dissolved in water residing on the cuticle surface (Pleim et al., 2013) or its pH (van Hove et al., 1989). In STAGE, R_{cut} is specified for wet periods (i.e., $R_{cut,wet}$) (i.e., macroscale wetness including rain and dew) and periods that are considered dry ($R_{cut,dry}$) but will include microscale wetness (i.e., thin layers on the cuticle surface) at high relative humidity (RH) (Table S2). Here we restrict our analysis to the role of $R_{cut,dry}$, as it dominates (78% of hourly periods) R_{cut}. R_{cut} cannot be measured directly, rather it is typically inferred from night-time canopy-scale NH_3 flux measurements under the assumption that the stomatal flux pathway is closed and the ground flux is negligible (Massad et al., 2010). Such datasets show a clear, generally non-linear, relationship with RH, indicating a reduction in $R_{cut,dry}$ as thin water layers form on the cuticle surface (Massad et al., 2010) at high RH. The minimum cuticular resistance ($R_{cut,min}$) demonstrates a relationship with pH of the cuticle surface water, parameterized as the ratio of total acid to NH_3 in the atmosphere (i.e., acid ratio, Nemitz et al., 2001). Here we assume an acid ratio of 1, yielding $R_{cut,min}$ = 31.5 (Massad et al., 2010). An empirical factor (α_{cut}) defines the form of the exponential relationship between $R_{cut,dry}$ and RH, thus exerting important control on the dynamics of F_{cut}.

Based on metanalysis of existing datasets, Massad et al. (2010) separate α_{cut} by ecosystem type based on the expectation that the factors controlling the relationship between RH and formation of microscale water layers on the cuticle, such as hygroscopicity and aerosol uptake, will differ by plant species (Massad et al., 2010). For forests, the mean and standard deviation of α_{cut} reported by Massad et al. (2010) are 0.0318 and 0.0179, respectively. In our analysis, the sensitivity of F_{net} to $R_{cut,dry}$ is assessed by varying α_{cut} by ± 0.0179, equivalent to a change of ± 56%. Increasing α_{cut} increases $R_{cut,dry}$, thereby decreasing NH_3 dry deposition by 0.28 kg N ha^{-1} (-20.3%) relative to the base case. Total dry N deposition is reduced by 10.2%, subsequently reducing the contribution of dry to total deposition from 39.5% to 36.9%. Decreasing α_{cut} decreases $R_{cut,dry}$, thereby increasing NH_3 dry deposition by 0.41 kg N ha^{-1} (29.7%) relative to the base case. Total dry N deposition increases by 15.9%, subsequently increasing the contribution of dry to total deposition from 39.5% to 43%.

Emission potentials (Γ) of the ground and vegetation are key inputs to the model, as they govern the surface compensations points and subsequently the direction and magnitude of the component (e.g., ground and canopy) and net canopy-scale fluxes. As described above, parametrization of the leaf and litter emission potentials based on bulk tissue chemistry contains uncertainty. While the magnitude of the uncertainty is not known, the sensitivity of the net canopy-scale flux to Γ can be assessed by varying the litter (Γ_l) and stomatal (Γ_s) emission potentials together and individually within the IQR of the observations (Table S8) assuming that uncertainty is ultimately less than naturally observed variability. Simultaneously reducing Γ_l and Γ_s to their corresponding 25th percentiles increases net NH_3 dry deposition by 0.07 kg N ha^{-1} (+5.1%) relative to the base case. Simultaneously increasing Γ_l and Γ_s to their corresponding 75th percentiles has a larger impact, decreasing NH_3 dry deposition by 0.65 kg N ha^{-1} (-47.1%) relative to the base case. Total dry N deposition is reduced by 24.2%, subsequently reducing the contribution of dry to total deposition from 39.5% to 33.0%. Adjusting Γ_l and Γ_s individually within their respective IQR while holding the other constant reveals a similar pattern. Larger responses are observed by increasing rather than decreasing Γ_l and Γ_s. Individually increasing Γ_l to the 75th percentile reduces NH_3 dry deposition by 37.0%, while increasing Γ_s reduces NH_3 dry deposition by 10.1%. This response reflects differences in the magnitude and variability of the measured Γ_l and Γ_s.

The ground flux (F_g) is controlled by Γ_g and the total ground resistance (R_g), which is the sum of R_{inc}, R_{bg} and soil (R_{soil}) resistances (Table S2). For NH_3, R_{soil} is a function of the length of the dry soil layer through which NH_3 originating from the soil solution must diffuse to the atmosphere (Sakaguchi and Zeng, 2009). As noted above, analysis of the soil and litter chemistry along with in-canopy profiles of NH_3 air concentration suggests that it is more appropriate to set the ground emission potential to that of the litter rather than the much more acidic underlying soil. We do so acknowledging that the physical process by which NH_3 diffuses from the litter layer to the atmosphere will differ from diffusion through the soil dry surface layer. However, while studies have investigated the potential role of leaf litter in NH_3 air-surface exchange above forests (Hansen et al., 2013; 2015), a parameterization for a litter layer resistance (R_{litter}) for forests has not been developed. Thus, we retain the current parameterization for R_{soil} and set $\Gamma_g = \Gamma_l$ to calculate compensation points and F_g in STAGE. To test the potential implications of substituting R_{litter} for R_{soil}, we assess the impact to F_{net} of changing R_{soil} by a factor of ±2. Doubling R_{soil} or reducing it by half has a minor

effect on NH_3 dry deposition equivalent to ± ~ 0.02 kg N ha^{-1} (~ ± 1.4%). This might be expected given that R_g depends not only on R_{soil} but also R_{inc} and R_{bg}. On average, R_{inc}, R_{bg}, and R_{soil} comprise 9.7%, 41.5%, and 48.8% of R_g (= R_{inc} + R_{bg} + R_{soil}) for NH_3.While development and implementation of a mechanistically representative R_{litter} to replace R_{soil} for forests is a necessary long-term goal, it is unlikely that it would dramatically alter the results presented here.

The final sensitivity scenarios relate to the assumption of the particle size distribution in the calculation of NH_4^+, NO_3^-, and PON fluxes. Three size distributions based on the data of Zhang et al. (2008) are shown in Supplemental Figure S10. The base STAGE model run assumes profile 1, which corresponds to the size distribution measured at clean sites of Zhang et al. (2008). Two more profiles (profile 2 and 3) were selected from the polluted sites for the purpose of sensitivity tests. Adopting profile 2 shifts the distribution to smaller sizes, increasing particulate V_d and subsequently increasing total dry N deposition but only by a very small amount (0.07 kg N ha^{-1} or 2.7%). Adopting profile 3 shifts the distribution to larger sizes, decreasing particulate V_d and subsequently decreasing total dry N deposition by an even smaller amount (<1%). Given the already much smaller V_d of particles relative to gases, the model results are relatively insensitive to assumptions of particle size distribution assumed in the V_d parameterization.

Table S11. Results of model sensitivity testing. Annual NH_3 dry deposition, total dry deposition, and total deposition (kg N ha^{-1}) are reported, along with contribution (%) of NH_3 dry deposition to total deposition and contribution of dry deposition to total deposition, for combinations of alternative model parameterizations and inputs relative to the base model scenario.

	NH_3_dry	Dry	Total	NH_3_dry	Dry
	kg N ha^{-1}	kg N ha^{-1}	kg N ha^{-1}	% of Total Dry	% of Total Wet + Dry
Base	1.38	2.64	6.70	52.1	39.5
LAI+30%	1.58	2.97	7.03	53.4	42.2
LAI-30%	1.13	2.26	6.32	49.8	35.8
$R_{cut,dry}$+	1.10	2.37	6.43	46.5	36.9
$R_{cut,dry}$-	1.79	3.06	7.12	58.5	43.0
$\Gamma_{s,l} = P_{25}$	1.45	2.72	6.78	53.4	40.1
$\Gamma_{s,l} = P_{75}$	0.73	2.00	6.06	36.6	33.0
$\Gamma_s = P_{50}, \Gamma_l = P_{25}$	1.43	2.70	6.76	52.9	39.9
$\Gamma_s = P_{50}, \Gamma_l = P_{75}$	0.87	2.14	6.20	40.6	34.5
$\Gamma_s = P_{25}, \Gamma_l = P_{50}$	1.40	2.67	6.73	52.5	39.7
$\Gamma_s = P_{75}, \Gamma_l = P_{50}$	1.24	2.51	6.57	49.4	38.2
R_{soil}x2	1.36	2.63	6.69	51.7	39.3
R_{soil}x0.5	1.40	2.66	6.73	52.4	39.6
PSD = Profile 2		2.71	6.77		40.0
PSD = Profile 3		2.64	6.70		39.4

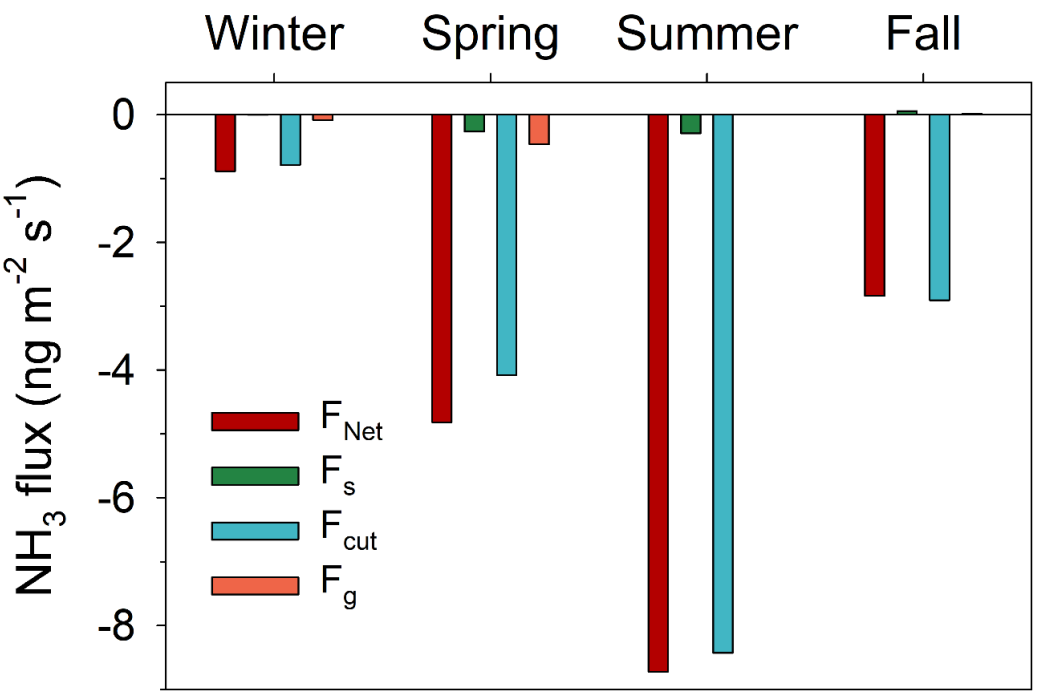

Figure S9. Seasonal mean net canopy-scale (F_{net}) and component (F_s = stomatal, F_{cut} = cuticular, F_g = ground) NH_3 fluxes from STAGE. Negative values indicate deposition.

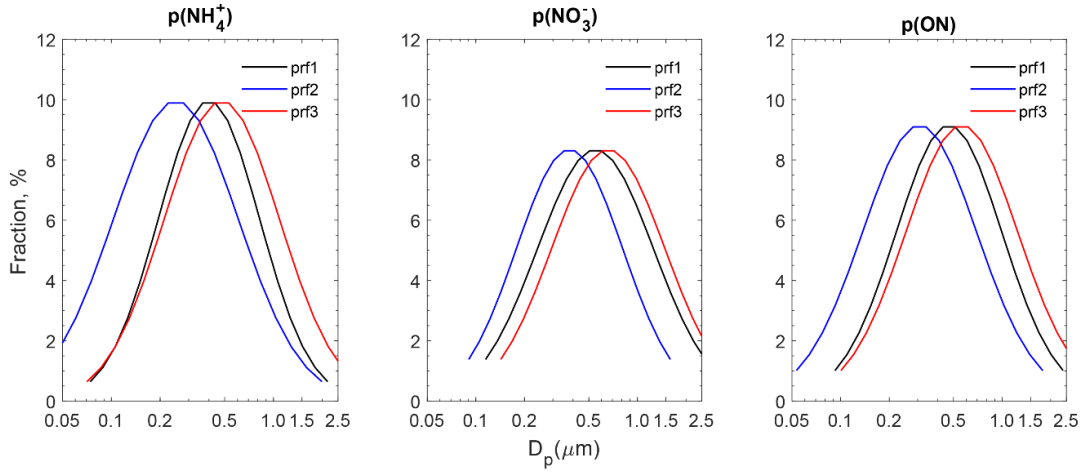

Figure S10. Particle size distributions used in the calculation of NH_4^+, NO_3^- and PON fluxes (prf1) and alternative profiles used to test model sensitivity (prf2 and prf3). Particle diameter (Dp) and corresponding fraction (%) of total particulate mass are shown. Note that the mass median aerodynamic diameter (MMAD) and geometric standard deviation (GSD) used to generate the size distributions for NH_4^+ and NO_3^- were from Table 5 of Zhang et al. (2008). PON was not measured at Zhang et al. (2008) and the values used here were taken as the mean of NH_4^+ and NO_3^-.

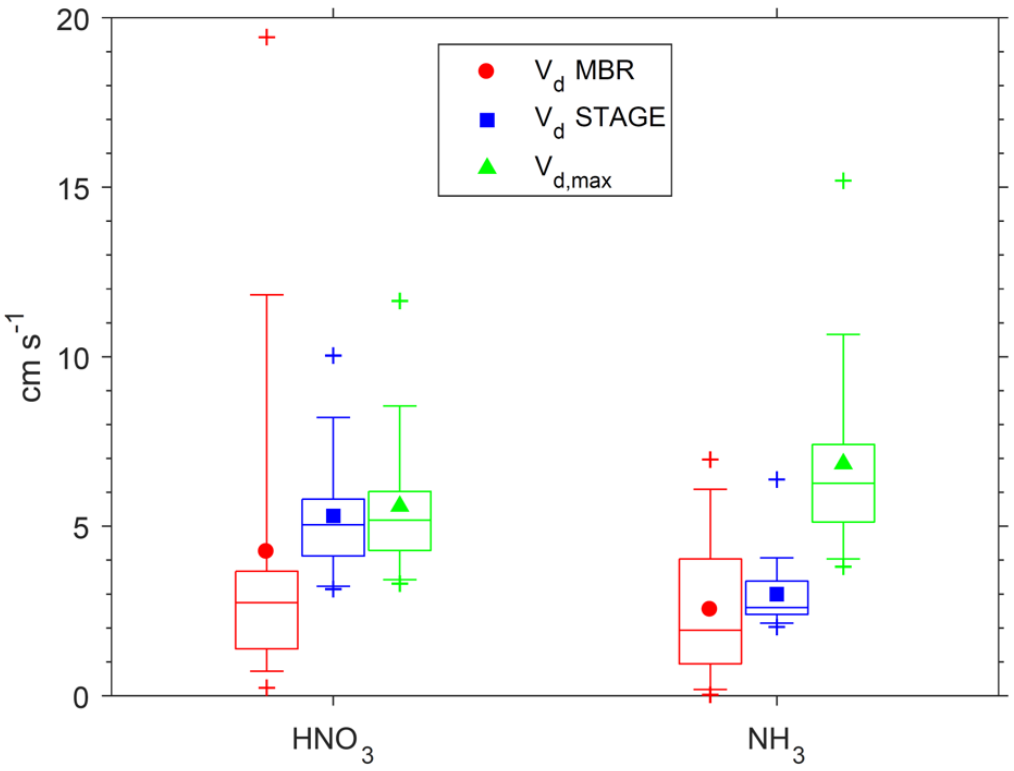

Figure S11. Box-plots of deposition velocity (V_d) estimated by modified Bowen ratio (MBR), STAGE model, and maximum V_d as $1/(R_a + R_b)$.

References

Breda, N., 2003. Ground-based measurements of leaf area index: a review of methods, instruments and current controversies. Journal of Experimental Botany, 54, 2403-2417.

Campbell, G.S., Norman, J.M., 1998. An Introduction to Environmental Biophysics. Springer, New York.

Hansen, K., Sørensen, L.L., Hertel, O., Geels, C., Skjøth, C.A., Jensen, B., Boegh, E., 2013. Ammonia emissions from deciduous forest after leaf fall. Biogeosciences, 10, 4577–4589.

Hansen, K., Personne, E., Skjoth, C.A., Loubet, B., Ibrom, A., Jensen, R., Sorenson, L.L., Beogh, E., 2017. Investigation sources of measured forest-atmospheric ammonia fluxes using tow-layer bi-directional modelling. Agricultural and Forest Meteorology, 237-238, 80-94.

Iiames, J., Congalton, R.G., Pilant, A., Lewis, T.E., 2008. Validation of an integrated estimation of Loblolly pine (Pinus taeda l.) leaf area index (LAI) utilizing two indirect optical methods in the southeastern United States. Southern Journal of Applied Forestry, 32, 101-110.

Leblanc, S., Chen, J.M., Fernandes, R., Deering, D.W., Conley, A., 2005. Methodology comparison for canopy structure parameters extraction from digital hemispherical photography in boreal forests. Agricultural and Forest Meteorology, 129, 187–207.

Martin, J.G., Kloeppel, B.D., Schaefer, T.L., Kimbler, D.L., McNulty, S.G., 1998. Aboveground biomass and nitrogen allocation of ten deciduous southern Appalachian tree species. Canadian Journal of Forest Research, 28, 1648–1659.

Massad, R.-S., Nemitz, E., Sutton, M., 2010. Review and parameterisation of bi-directional ammonia exchange between vegetation and the atmosphere. Atmospheric Chemistry and Physics, 10, 10359-10386.

Myneni, R.B., Hoffman, S., Knyazikhin, Y., Privette, J.L., Glassy, J., Tian, Y., Wang, Y., Song, X., Zhang, Y., Smith, G.R., Lotsch, A., Friedl, M., Morisette, J.T., Votava, P., Nemani, R.R. and Running, S.W., 2002. Global products of vegetation leaf area and fraction absorbed PAR from year one of MODIS data. Remote Sensing of Environment, 83, 214-231.

Nemitz, E., Milford, C., Sutton, M.A., 2001. A two-layer canopy compensation point model for describing bi-directional biosphere-atmosphere exchange of ammonia. Quarterly Journal of the Royal Meteorological Society, 127, 815-833.

Oishi, A.C., Miniat, C.F., Novick, K.A., Brantley, S.T., Vose, J.M., Walker, J.T., 2018. Warmer temperatures reduce net carbon uptake, but not water use in a mature southern Appalachian forest. Agricultural and Forest Meteorology, 252, 269-282.

Pleim, J.E., Bash, J.O., Walker, J.T., Cooter, E.J., 2013. Development and evaluation of an ammonia bi-directional flux parameterization for air quality models. Journal of Geophysical Research - Atmospheres, 118, 3794–3806.

Sakaguchi, K., Zeng, X., 2009. Effects of soil wetness, plant litter, and under-canopy atmospheric stability on ground evaporation in the Community Land Model (CLM3.5). Journal of Geophysical Research - Atmospheres, 114, D01107.

van Hove, L.W.A., Adema, E.H., Vredenberg, W.J., Pieters, G.A., 1989. A study of the adsorption of NH_3 and SO_2 on leaf surfaces. Atmospheric Environment, 23, 1479–1486

Zhang, L., R. Vet, A. Wiebe, C. Mihele, B. Sukloff, E. Chan, M. D. Moran, S. Iqbal., 2008. Characterization of the size-segregated water-soluble inorganic ions at eight Canadian rural sites. Atmospheric Chemistry and Physics, 8, 7133-7151.